AGU PUBLICATIONS

Geochemistry, Geophysics, Geosystems

RESEARCH ARTICLE
10.1002/2013GC005172

Central Cascadia subduction zone creep

Gina M. Schmalzle[1,2], Robert McCaffrey[3], and Kenneth C. Creager[1]

[1]Earth and Space Sciences, University of Washington, Seattle, Washington, USA, [2]Now at BOS Technologies, LLC, Seattle, Washington, USA, [3]Department of Geology, Portland State University, Portland, Oregon, USA

Key Points:
- Cascadia locking, slow-slip, and coseismic subsidence are compared to terranes
- Reduced Cascadia interseismic uplift and coseismic subsidence suggest creep
- Increased pore fluid pressures under Siletzia terrane encourage creep

Supporting Information:
- Readme
- Figures S1-S13
- Tables T1-T11

Correspondence to:
G. M. Schmalzle,
gina@bostechnologies.com

Citation:
Schmalzle, G. M., R. McCaffrey, and K. C. Creager (2014), Central Cascadia subduction zone creep, *Geochem. Geophys. Geosyst.*, *15*, 1515–1532, doi:10.1002/2013GC005172.

Received 4 DEC 2013
Accepted 11 MAR 2014
Accepted article online 14 MAR 2014
Published online 30 APR 2014

Abstract Central Cascadia between 43°N and 46°N has reduced interseismic uplift observed in geodetic data and coseismic subsidence seen in multiple thrust earthquakes, suggesting elevated persistent fault creep in this section of the subduction zone. We estimate subduction thrust "decade-scale" locking and crustal block rotations from three-component continuous Global Positioning System (GPS) time series from 1997 to 2013, as well as 80 year tide gauge and leveling-derived uplift rates. Geodetic observations indicate coastal central Oregon is rising at a slower rate than coastal Washington, southern Oregon and northern California. Modeled locking distributions suggest a wide locking transition zone that extends inland under central Oregon. Paleoseismic records of multiple great earthquakes along Cascadia indicate less subsidence in central Oregon. The Cascade thrust under central Oregon may be partially creeping for at least 6500 years (the length of the paleoseismic record) reducing interseismic uplift and resulting in reduced coseismic subsidence. Large accretions of Eocene age basalt (Siletzia terrane) between 43°N and 46°N may be less permeable compared to surrounding terranes, potentially increasing pore fluid pressures along the fault interface resulting in a wide zone of persistent fault creep. In a separate inversion, three-component GPS time series from 1 July 2005 to 1 January 2011 are used to estimate upper plate deformation, locking between slow-slip events (SSEs), slip from 16 SSEs and an earthquake mechanism. Cumulative SSEs and tectonic tremor are weakest between 43°N and 46°N where partial fault creep is increased and Siletzia terrane is thick, suggesting that surrounding rock properties may influence the mode of slip.

1. Introduction

Knowledge of locking, or the amount the overriding plate is stuck (locked) to the subducting oceanic plate, is critical for estimating seismic hazard of subduction zones because greater locking may indicate greater potential for larger earthquakes. Complicating our understanding of locking, many subduction zones have slow-slip events that occur over a period of days to months along sections of the plate boundary that release and redistribute part of the stress built up in the subduction zone during the earthquake cycle. Slow-slip events (SSEs) have been reported at subduction zones in southwest Japan [*Heki et al*., 1997; *Hirose et al*., 1999; *Ozawa et al*., 2001], Mexico [*Lowry et al*., 2001], Costa Rica [*Outerbridge et al*., 2010], Kamchatka [*Burgmann et al*., 2001], Alaska [*Freymueller et al*., 2002], New Zealand [*Douglas et al*., 2005], and Cascadia [*Dragert et al*., 2001]. SSEs in Cascadia and other (but not all) subduction zones are often accompanied by tectonic tremor and where they occur together are named episodic tremor and slip (ETS) [*Rogers and Dragert*, 2003]. Another mode of interearthquake slip is persistent fault creep, which differs from SSEs in that the motion is steady over the earthquake cycle.

In northern California, the Pacific plate moves northwest relative to North America at about 50 mm/yr [*Atwater*, 1970; *DeMets and Dixon*, 1999]. North of the Mendocino Triple Junction (MTJ), the young Gorda and Juan de Fuca plates subduct beneath the North America plate at about 30 mm/yr offshore northern California which steadily increases to about 45 mm/yr offshore Vancouver Island, Canada [*Wilson*, 1993]. Unlike the smooth transition in convergence rate from south to north, locking patterns inferred from geodetic data vary. These variations are partly real but also reflect assumptions in how locking is defined in the geodetic model [*Hyndman and Wang*, 1993; *McCaffrey et al*., 2000; *Miller et al*., 2001; *Wang et al*., 2003; *McCaffrey et al*., 2007; *Burgette et al*., 2009; *McCaffrey*, 2009; *McCaffrey et al*., 2013]. SSE recurrence in Cascadia also varies latitudinally [*Brudzinski and Allen*, 2007; *Szeliga et al*., 2008]. Using networks of GPS and seismometers, *Brudzinski and Allen* [2007] demonstrate that ETS occur about once every 14 months in Washington, once every 2 years in central and northern Oregon, and about every 10 months in northern California. The

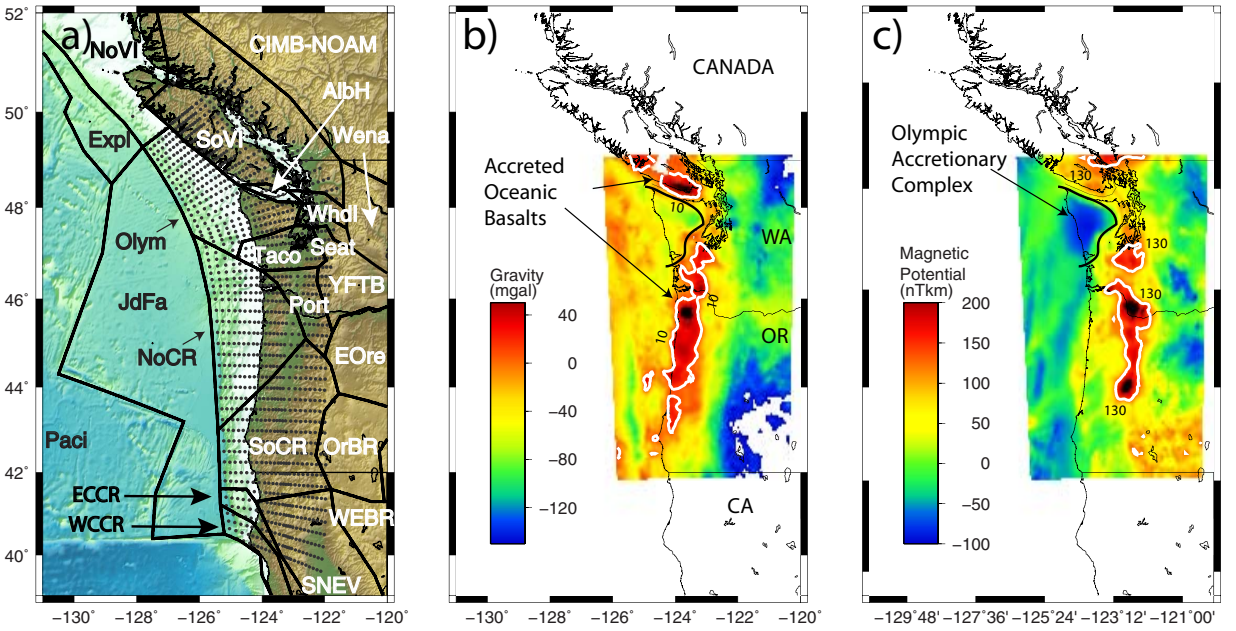

Figure 1. Model setup with (a) named blocks, (b) gravity, and (c) magnetic potential data sets. (Figure 1a) Block boundaries (black lines) based on *McCaffrey et al.* [2007]. Blocks CIMB and NOAM are combined. Dots are nodes that make up the plate boundary interface. Node depths based on *McCrory et al.* [2004]. (Figure 1b) Bouguer gravity anomalies (onshore) and free-air anomalies (offshore) from *Blakely et al.* [2005]. White outline marks the 10 mgal contour and maps the spatial extent of the thickest accretions of the dense Siletzia terrane. (Figure 1c) Aeromagnetic anomalies transformed to magnetic potential from *Blakely et al.* [2005]. White outline marks the 130 nT km contour and maps the spatial extent of the magnetized body inferred as serpentinized mantle. Aeromagnetic anomalies are notably reduced in the Olympic accretionary complex (black outline).

observation that the amount of locking and slow-slip in Cascadia do not follow the same along-strike trend as the increase in plate convergence rate [e.g., *McCaffrey et al.*, 2013] suggests they must be influenced by properties at or near the fault surface [*Schwartz and Rokosky*, 2006; *Brudzinski and Allen*, 2007; *Reyners and Eberhart-Phillips*, 2009; *Audet et al.*, 2010; *Peng and Gomberg*, 2010].

We use margin-wide continuous Global Positioning System (GPS) as well as tide gauge and leveling-derived uplift rates to estimate the margin-wide distribution of locking and cumulative slow-slip. These estimates are compared to coseismic subsidence derived from paleoelevation studies and geologic distributions to understand Cascadia subduction mechanics. Our models extend as far south as the Mendocino Triple Junction (MTJ) in California, and provide the first estimates of slow-slip for this region (Figure 1a). Our results show that central Oregon between 43°N and 46°N has reduced interseismic uplift, coseismic subsidence, cumulative tremor and slow-slip. These observations can be explained by partial but persistent fault creep in the Cascadia thrust under central and northern Oregon where the thickest accumulations of dense Eocene age basalt called the Siletzia terrane exist (Figures 1b and 1c). We expand on a conceptual model that suggests the Siletzia terrane, if impermeable, may help accommodate persistent fault creep by increasing pore fluid pressure along the fault interface, ultimately influencing Cascade wide seismic hazard. Other explanations are also explored.

2. Geophysical Observations

2.1. Continuous GPS Time Series

Daily positions for continuous GPS sites in the Pacific Northwest are publicly available from Central Washington University (CWU) for the Pacific Northwest Geodetic Array (PANGA, http://www.geodesy.cwu.edu/) and from UNAVCO for the Plate Boundary Observatory (PBO, http://pbo.unavco.org/data/gps) [*Anderson et al.*, 2006] and are computed in the Stable North America Reference Frame [*SNARF Working Group*, 2004]. We use both PANGA and PBO time series, which provide a spatially more complete data set than either alone.

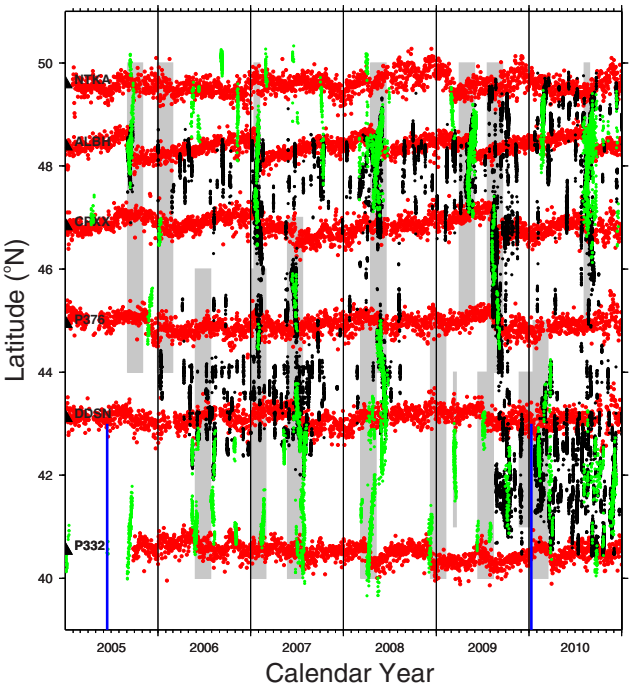

Figure 2. Tectonic tremor latitude as a function of time from the PNSN (black dots) and MU (green dots) catalogs. Latitudes of GPS sites NTKA, ALBH, CPXX, P376, DDSN, and P332 (triangles) mark where they are in relation to tremor and east component position time series (red dots) are superimposed. Vertical gray-shaded boxes indicate when and where our SSE model detects slow-slip episodes. Vertical blue lines mark the time of the 2005 and 2010 Eureka earthquakes. The SSE model includes events from 2005.5 to 2011.0.

2.2. Tide Gauge and Leveling-Derived Uplift Rates

We use 587 uplift rates determined by tide and leveling data from *Burgette et al*. [2009]. These data were obtained from six NOAA tide gauges that include observations from 1925 to 2006 and coastal leveling surveys done by the National Geodetic Survey (NGS) in the early 1930s, 1941, and in the late 1980s.

2.3. Tectonic Tremor Locations

Tectonic tremor is an emergent signal devoid of obvious impulsive arrivals presumably generated near the plate interface during slow-slip. In order to examine the relationship of tectonic tremor to GPS-detected slow-slip and to other features of the margin, we use tectonic tremor locations provided by the Pacific Northwest Seismic Network (PNSN, http://www.pnsn.org/tremor) based on methods described by *Wech and Creager* [2008] and *Wech* [2010]. The PNSN catalog is intermittent in time and space until mid 2009, when the network became fully operational margin wide. We supplement the PNSN catalog with the Miami University (MU) tremor catalog, described in *Boyarko and Brudzinski* [2010] and *Brudzinski and Allen* [2007]. Because these two catalogs cover different times and regions, we combine them to get the most complete record from 2005.5 to 2011.0. The catalogs indicate periods of elevated tremor throughout the margin (Figure 2). Most major slow-slip events detected by GPS have spatially and temporally associated tremor (Figure 2).

3. Methods

We present three models of Cascadia: two that represent the distribution of "decade-scale" locking without estimating slow-slip (decade-scale models) and a third that simultaneously estimates inter-SSE locking and slow-slip (the SSE model). "Decade scale" refers to the GPS time series duration ($\sim$10 years). Decade-scale models are used to estimate the along-strike pattern in the locking fraction whereas the SSE model is used to estimate along-strike pattern in cumulative slow-slip from 2005.5 to 2011.0. The decade-scale and SSE models are estimated using the program TDEFNODE [*McCaffrey*, 2002, 2009]. Our structural models are based on block models presented in *McCaffrey et al*. [2007] and *McCaffrey* [2009]. In all models, we divide the crust into 28 blocks shown in Figure 1a. Blocks with a limited number of stations or with no stations (SEOr, SWId, NoVI, SnRP, Paci, JdFa, Expl, and EBnR) are assigned the angular velocity given in *McCaffrey et al*. [2007], otherwise the rotations (Euler poles, three parameters per block) are estimated. Permanent strain rates within the YFTB, ECCR, and WCCR blocks are estimated by solving for the three components of a uniform spherical strain rate tensor [*Savage et al*., 2001].

The plate boundary fault is represented by a three-dimensional irregular grid of node points that define its shape (Figure 1a) and is based on the fault interface presented in *McCrory et al*. [2004]. Surface deformation due to slip on faults in an elastic half-space follows the routines of *Okada* [1985, 1992]. The locking fraction, ϕ, describes how much the plates are coupled, or locked, where $\phi = 0$ indicates no locking (free slip), and

$\phi = 1$ indicates the plates are completely locked. Alternatively, ϕ can be thought of as a creep fraction, where $\phi = 0$ is full creep, and $\phi = 1$ is no creep.

Rows of nodes are paired along strike in the inversion, effectively increasing node spacing (Figure 1a, dots) and reducing the number of free parameters. The best fit parameters are estimated by minimizing the penalty function:

$$\mathbf{R}^T\mathbf{W}\mathbf{R} + \alpha \sum_{i=1,N} \left(\frac{d^2\phi_i}{dx^2}\right)^2 + \beta \sum_{i=1,N} \left(\frac{\phi_i}{N}\right) + \sum \mathbf{P}_k \quad (1)$$

where **R** is the data residual vector, **W** is the weight matrix, α and β are scaling factors for damping, ϕ is the locking fraction (value between 0 and 1), N is the number of nodes, and $\mathbf{P}_k$ represents other penalties. The first term is the χ^2 data misfit, the second is along-strike smoothing, and the third damps the total slip rate deficit. This equation corrects a typo in equation (1) of *McCaffrey et al*. [2013]. For both decade-scale and SSE models, we use $\alpha = 10^7$ and $\beta = 0.2$. Model parameters are estimated by a combination of simulated annealing and grid search to minimize the penalty function (1) [*McCaffrey*, 2005].

3.1. Decade-Scale Velocities and Model Locking

Decade-scale velocities are dependent on site occupation histories since each site has been in operation at different times and may have recorded different slow-slip events. Hence, nearby sites may have different decade-scale velocities if they were operating at different times. GPS decade-scale velocities are calculated before they are applied to decade-scale models by estimating the position time series slope (1997–2012) for each component after removing seasonal effects, earthquakes, and equipment changes but not slow-slip events. We do not account for offsets due to SSEs in the decade-scale velocities because we are estimating average site velocities over the duration of the time series. The decade-scale site velocity **v** is calculated by fitting the time series (least squares) with the linear equation:

$$\mathbf{p}(t_i) = \mathbf{p}_o + \mathbf{v}^* t_i + \sum_{j=1}^{N} \boldsymbol{A}_j \boldsymbol{H}(t_i - t_j) + \mathbf{U_1} \sin(2\pi t_i) + \mathbf{U_2} \cos(2\pi t_i) + \mathbf{U_3} \sin(4\pi t_i) + \mathbf{U_4} \cos(4\pi t_i) \quad (2)$$

where $\mathbf{p}_o$ is the initial position of the time series, **v** is the decade-scale velocity (slope), ***H*** is a Heaviside step function that accounts for j = 1 to N events (earthquakes, equipment changes, etc.) at time t_j with amplitude $\boldsymbol{A}_j$, and $\mathbf{U_1}$, $\mathbf{U_2}$, $\mathbf{U_3}$, and $\mathbf{U_4}$ are coefficients for annual and semiannual seasonal signals. Velocity uncertainties are estimated as 3.0 mm divided by time series duration for horizontal velocities and 6.0 mm divided by time series duration for vertical velocities. Uncertainties $<$0.3 mm/yr are given the value of 0.3 mm/yr in the decade-scale inversion. The decade-scale velocity model inversion uses 720 CWU PANGA decade-scale rates (three components for 240 sites) and 420 PBO decade-scale rates (three components for 140 sites). Tide and leveling uplift rates (587 total) are also used in the decade-scale inversion. Decade-scale velocities are provided in supporting information.

Predicted GPS vertical rates and tide and leveling gauge uplift rates are systematically offset from each other. We adjust the GPS vertical reference frame by calculating the mean residual of the vertical rates relative to the model, which is then subtracted from the vertical GPS rates. PANGA and PBO vertical rates are shifted by -1.01 and -1.18 mm/yr, respectively. The inversion is performed again with these adjustments in the final decade-scale models.

Locking at most oceanic subduction zones is difficult to estimate because locking is typically offshore where there is rarely instrumentation to observe surface deformation. Knowing the locking distribution is important for seismic hazard estimates, however, since future coseismic rupture may occur where the plate interface is currently locked and assumptions of the locking distribution can greatly affect estimates of loading rates [*McCaffrey et al*., 2013]. At Cascadia, onshore measurements of deformation from survey-mode and continuous GPS [*McCaffrey et al*., 2000; *Wang et al*., 2003; *McCaffrey et al*., 2007; *McCaffrey*, 2009; *McCaffrey et al*., 2013] and tide and leveling data [*Hyndman and Wang*, 1993; *Burgette et al*., 2009; *McCaffrey et al*., 2013] have been used to estimate variations in margin-wide locking. In Cascadia, *Hyndman and Wang* [1993], *Flück et al*. [1997], and *Wang et al*. [2003] use thermal data to argue that the subduction zone is fully

locked near the trench and locking decreases according to an exponential decay function to freely slipping between the 350 and 450°C isotherms. A joint inversion of geodetic and tsunami data of the 2011 Tohoku-Oki earthquake suggests that rupture occurred near the trench over a large area, but slip appeared to have a Gaussian-like distribution [*Romano et al*., 2012]. Hence, similar to *McCaffrey et al*. [2013], we describe locking in two ways and compare the resulting distributions. The first approach uses a Gaussian distribution of ϕ with depth z [*McCaffrey et al*., 2013, paragraph 23] where $\phi(z) = A\exp\{-\frac{1}{2}[(z-Z_m)/Z_s]^2\}$ and the unknowns are A, a scalar, and Z_m and Z_s, the mean depth and spread of the locking distribution, respectively. We apply penalties to keep mean locking depths between 0 and 30 km depth. This model is referred to as the Gaussian decade-scale model. The second locking distribution assumes that the subduction zone is locked at the trench to some distance downdip where it transitions monotonically from fully locked to freely slipping by the shape factor gamma described in *Wang et al*. [2003] and *McCaffrey et al*. [2007]. The unknowns for this model are gamma and the depths at which the transition begins and ends. The second model is referred to as the Gamma decade-scale model. Decade-scale models use all three components of the GPS velocities, tide gauge, and leveling uplift rates to estimate block rotations, permanent block strain rates, and locking and have 141 free parameters. The modeled region ranges 120°W–130°W and 40°N–50°N.

3.2. GPS Time Series and SSE Model

Slow-slip events that are visually obvious in the time series are examined in this study and are among the largest between 2005.5 and 2011.0. Many tremor swarms occur throughout the time between large SSEs, and occur further downdip than larger tremor swarms [*Wech and Creager*, 2011]. We argue that the consistency of the GPS time series slopes between large SSEs suggests that smaller SSEs do not contribute much to the cumulative SSE moment or contribute at a relatively constant rate. The consistency of the inter-SSE velocities also suggests that there is no long-period event occurring, such as a $M \geq 8$ SSE [*Meade and Loveless*, 2009]. We use the east component of the GPS time series (with the trend and seasonal signals removed) and elevated tremor counts to visually determine when major slow-slip events occurred along the margin (e.g., Figure 2). Similar to the observations of *Brudzinski and Allen* [2007], SSEs are observed approximately every 12–14 months north of 47°N and are noticeably less frequent from 46°N to about 41°N (Figures 3a and 3b). Between 40°N and 41°N, slow-slip events occur most frequently along the margin every 10–12 months (Figure 3b). Events are not obvious south of 39.9°N for the time period of this study (Figure 3b). In all, 16 events produced noticeable offsets in the GPS time series.

We decimate the daily position time series between 1 July 2005 and 1 January 2011 to one sample every 7 days to reduce computation time. In total we use 240 CWU PANGA and 154 PBO stations, of which 258 are unique. Sixty-nine unique stations provided daily position estimates for 90% or more of time period observed, and 114 unique stations provided position estimates for 80% or more of the time studied. The CWU PANGA time series are rotated into the PBO reference frame. We do not use tide gauge and leveling velocities in the SSE model because these data reflect the longer-term average velocity, rather than the short-term interSSE velocities.

The SSE model uses the decimated GPS position time series directly to solve for inter-SSE block Euler poles, permanent horizontal block strain rates, fault locking, and transient events including slow-slip, after slip, and earthquakes. The time series of position X is given by

$$\mathbf{X}^k(t) = \mathbf{X}_o{}^k + \mathbf{V}(\mathbf{x}^k)^* t + \mathbf{S}^k(t) + \mathbf{T}(\mathbf{x}^k, t) \quad (3)$$

where $\mathbf{X}^k(t)$ is the predicted time-dependent position vector of the kth station, $\mathbf{X}_o^k$ is the initial position vector of the kth station (estimated), $\mathbf{V}$ is the steady intertransient velocity vector evaluated at the position of the kth station ($\mathbf{x}^k$) (estimated), $\mathbf{S}$ is the seasonal vector-valued signal comprising annual and semiannual terms $\mathbf{U}$ (see equation (2); estimated), and $\mathbf{T}$ represents the time series due to transients, which are calculated for one earthquake and 16 SSEs. Steady site velocities, $\mathbf{V(x)}$, are calculated from inter-SSE steady block rotations, block strain rates, and elastic deformation rates associated with plate boundary fault locking. Site velocities are spatially correlated through block model parameters and locking in $\mathbf{V}(\mathbf{x})$ and through transient slip described in $\mathbf{T}(\mathbf{x},t)$.

Inter-SSE locking differs from the decade-scale locking because it is derived from the slope of the position time series (the velocity) between SSEs, rather than from the slope of the entire time series with SSEs

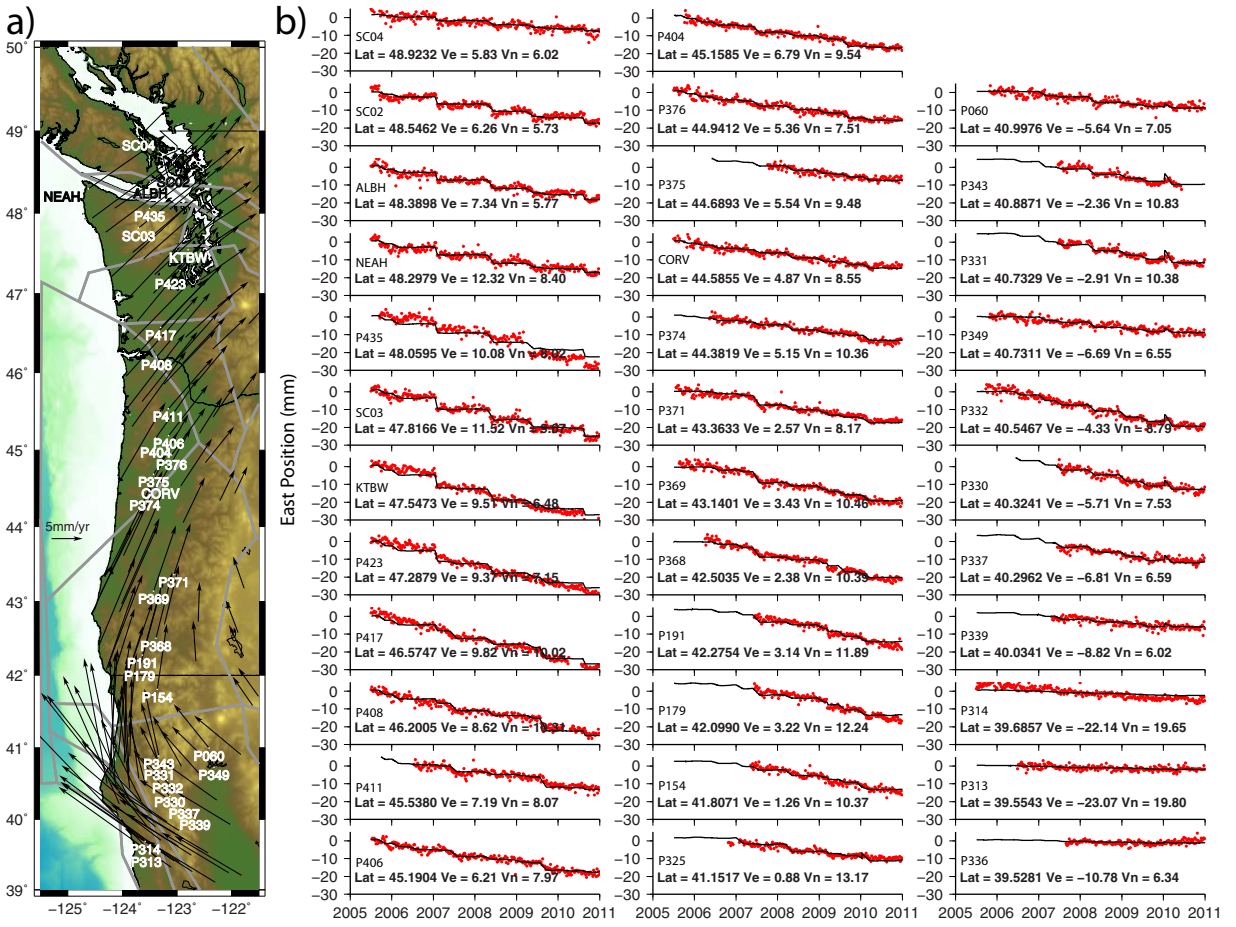

Figure 3. (a) Map of inter-SSE GPS velocities (black arrows) and (b) select PBO GPS east component position (mm) time series (red dots) and SSE model fit (black line) detrended by their predicted velocities. Site names are superimposed on the map and labeled on the respective position time series. Time series plots include the latitude (Lat) and the east and north components of the inter-SSE velocity (Ve and Vn, respectively) in mm/yr.

included. We parameterize the inter-SSE locking fraction as a Gaussian function of depth, in the same way as in the Gaussian decade-scale model.

Our SSE model extends from 39.5°N to 49.5°N (Figure 3). We describe the spatial distribution of slow-slip as a Gaussian function of depth. Similar to locking, along-strike rows of nodes are paired in slow-slip inversions, but a zero displacement boundary condition on the southern-most and northern-most rows of nodes is enforced. The regularization parameters for slow-slip events are $\alpha = 10^7$ and $\beta = 0.2$ (equation (1)). The time dependence of slow-slip velocity is a boxcar function that results in a linear ramp in displacement, starting at time t_o with a duration t_c.

We estimate by eye start times of 16 slow-slip events but let them and their durations adjust in the inversion. To reduce the number of free parameters, we modeled southern and northern SSEs separately with a boundary at 44°N unless tremor and/or GPS time series indicate the SSE extended past this latitude. We assign slow-slip direction as opposite inter-SSE relative motion on the fault derived from block motions. For each event, we constrain the start time to ±0.1 year of the picked start time, the duration to between 10 and 60 days, the amplitude to <200 mm, the peak Gaussian slip to 20 and 60 km depth, and the Gaussian spread to 5–100 km. If modeled parameters fall outside these ranges, penalties are applied by taking the absolute value of the difference between the parameter value and the limit of the allowed range and multiplying it by 10 (equation (1)).

The 9 January 2010 Eureka earthquake is observed in the GPS position time series. It is defined in the model by uniform slip on a planar fault. The latitude, strike, and amplitude are adjusted while all other parameters (longitude, dip, and rake) are set to the Berkeley moment tensor solution (Table 1). The earthquake time

Table 1. Berkeley Solution (BRK) for the 2010 Eureka Earthquake

Longitude (°E)	Latitude (°N)	Depth (km)	Strike (°)	Dip (°)	Rake (°)	Mw
−124.692	40.652	24.0	230.0	86.0	11.0	6.5

dependence is an impulse because time sampling of continuous GPS is daily and the earthquake lasted only a few seconds.

Block WCCR in northern California is deforming rapidly and in a complex manner, and cannot be matched well by a uniform internal block strain rate. We remove sites CME1, P157, P163, P156, P315, and P317, which reside on the southwestern side of the block, and recognize that the southwestern corner of our SSE model is not well constrained.

4. Results

4.1. Decade-Scale Results

The decade-scale horizontal velocity field relative to North America is directed to the northwest in California and rotates northward in central Oregon, and to the northeast in Washington and Canada (Figure 4a). This pattern has been observed in earlier geodetic studies [e.g., *McCaffrey et al.*, 2000; *Miller et al.*, 2001; *McCaffrey et al.*, 2007, 2013] and is attributed to the rotation of Oregon [*Wells et al.*, 1998] driven by the northwesterly motion of the Basin and Range, the convergence of the Juan de Fuca plate and other forces. The east components of the horizontal velocities are large near the coast and decrease inland, consistent with locking-induced strain (Figures 4a–4g, S1a, and S1b). GPS, tide gauge, and leveling indicate ~3–4 mm/yr uplift rates near the coast in Washington and southern Oregon that taper to zero inland (Figures 5a, 5c–5h, S2a, and S2b). Coastal northern and central Oregon, however, has little uplift (0–1 mm/yr, Figures 5a and 5c–5h) [*Mitchell et al.*, 1994; *Burgette et al.*, 2009]. Horizontal velocities are fit well in both decade-scale

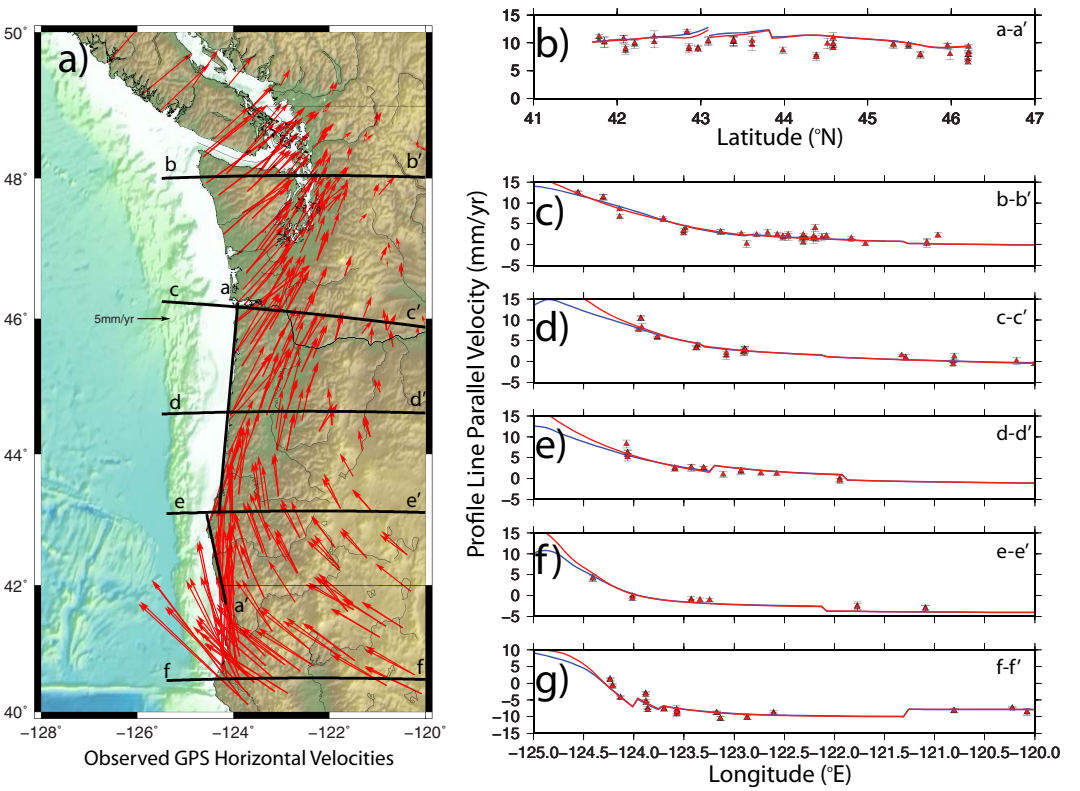

Figure 4. (a) Map of observed horizontal GPS velocities that includes profile lines. (Figures 4b–4g) Decade-scale profile line parallel horizontal GPS velocities (triangles with one-sigma uncertainties) and decade-scale modeled velocities for the Gamma (red line) and Gaussian (blue line) models for profiles a-a′ (b), b-b′ (c), c-c′ (d), d-d′ (e), e-e′ (f) and f-f′ (g).

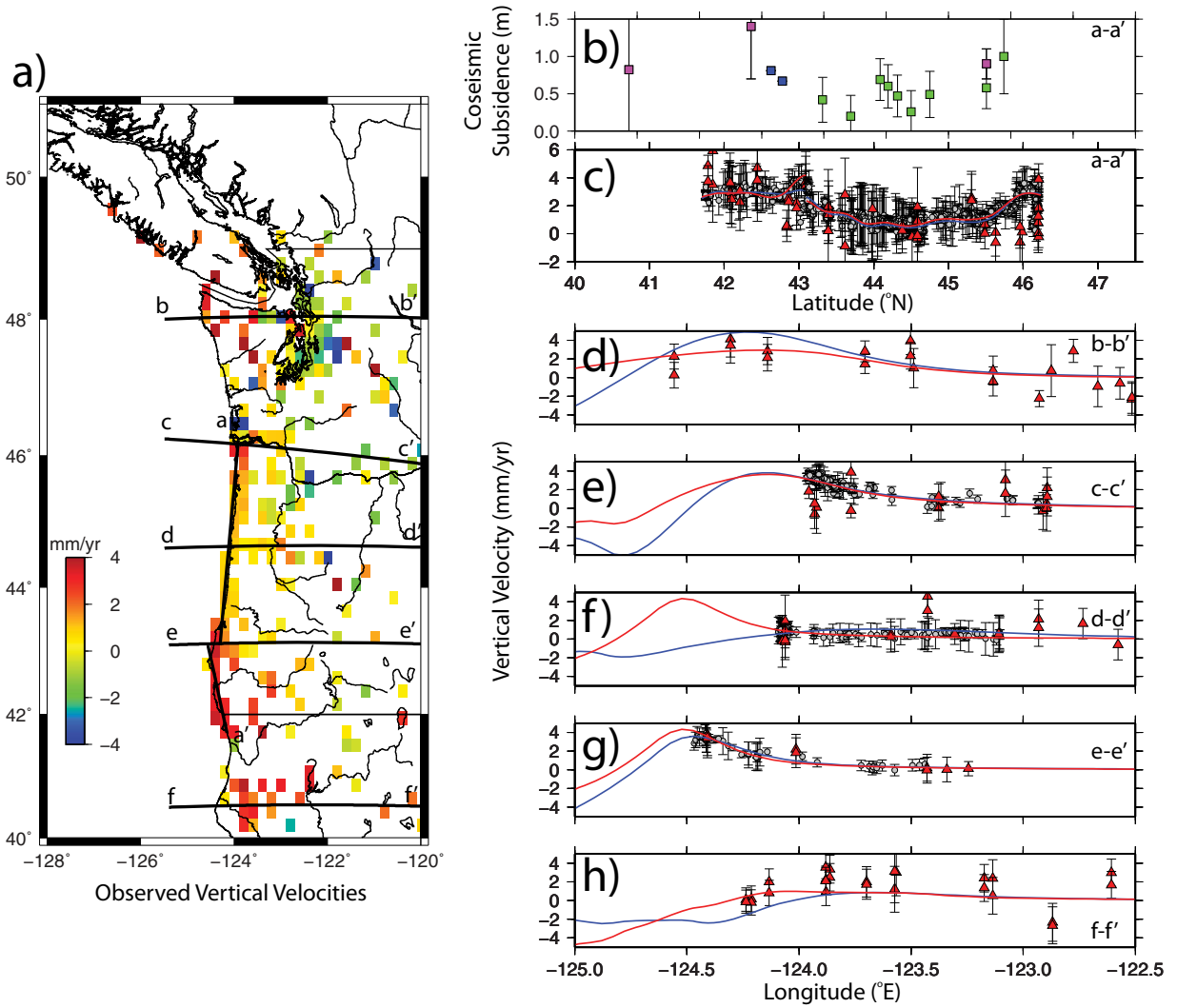

Figure 5. (a) Map of observed geodetic vertical rates with profile lines. (b) Coseismic subdsidence from the 1700 earthquake along profile a-a′. Squares are standard deviations (green), minimum estimates (blue), and estimate ranges (purple) from the coseismic data set in *Wang et al.* [2013]. (Figures 5c–5h) Decade-scale interseismic vertical velocity profiles including GPS uplift rates (triangles with one-sigma uncertainties), tide and leveling uplift rates (gray circles with 1-sigma uncertainties), and decade-scale modeled vertical velocities for the Gamma (red line) and Gaussian (blue line) models for profiles a-a′ (c), b-b′ (d), c-c′ (e), d-d′ (f), e-e′ (g) and f-f′ (h).

models, but vertical GPS rates are systematically misfit in northern California (Figures S1 and S2). Northern California had several magnitude 6 or greater earthquakes within the past 100 years, including the most recent M > 6 Eureka earthquakes in 2005.45 (prior to the time period of this study) and 2010.02. Continuous GPS vertical time series show little postseismic motion during these primarily strike-slip events. Hence, we expect that postseismic motion is not the source of the vertical anomalies. Our models assume the plate geometry of *McCrory et al*. [2004]. An updated plate geometry model reveals more complex structure in southern Cascadia [*McCrory et al*., 2012]. We test the influence of the new geometry by running the Gaussian locking model again with the updated plate geometry. Horizontal and vertical misfits are not changed significantly using the new geometry (Figure S3).

Fitting decade-scale velocities with the Gaussian and Gamma models achieve reduced χ^2 of 1.55 and 1.61, respectively, each with the same number of free parameters (Table 3). Both decade-scale models estimate locking fraction and slip rate deficit distributions that show a wide locking transition zone between ~43°N and 46°N and at ~41°N (Figures 6a, 6b, S4a, and S4b). The modeled locking distribution is substantially different offshore since it is dependent on the model assumptions, but the two models are similar onshore (Figures 4–6). The estimated moment rate per unit length is the sum of the slip rate deficit times fault area

Table 2. Detected Events From This Study Compared to Other Works

Start Date (This Study, YYYY/MM/DD)	End Date (This Study, YYYY/MM/DD)	Detection Area[a]	Mw (This Study)	Other Work (Mw)[b]
2005/9/4[c]	2005/11/2	W,O	6.74	SG(6.7), BB
2005/12/30[c]	2006/2/28	W,O	6.73	SG(6.2), BB
2006/5/29	2006/7/27	O,C	6.78	BB
2007/1/1	2007/2/29	O,C	6.66	BB
2007/1/15	2007/2/5	W	6.86	SG(6.6)
2007/5/26	2007/7/24	O,C	6.99	SG(6.2), BB
2008/3/10	2008/5/9	O,C	6.81	N/A
2008/4/18	2008/6/17	W,O	6.86	SG(6.6)
2008/12/9	2009/2/7	O,C	6.71	N/A
2009/4/2	2009/5/31	W	6.76	N/A
2009/3/10	2009/3/20	O	6.43	N/A
2009/6/14	2009/8/12	O,C	6.72	N/A
2009/7/21	2009/9/19	W,O	6.84	N/A
2009/11/24	2010/1/23	O,C	6.51	N/A
2010/1/17	2010/3/16	O,C	6.81	N/A
2010/8/6	2010/8/27	W,O	6.86	N/A

[a]Washington (W), Oregon (O), or California (C).
[b]Other works include *Boyarko and Brudzinski* [2010] (BB) and *Schmidt and Gao* [2010] (SG). Moment magnitude in parentheses if reported in other works.
[c]SSEs are close in time and space at the beginning of the evaluated time series and are poorly resolved.

times rigidity (40 GPa) divided by the along-strike distance. In the Gamma decade-scale locking model, the moment rate per unit length is substantially larger than in the Gaussian locking distribution (Figure 6c). Separating the moment rate per unit length to depths greater and less than 20 km (the approximate depth of the slab under the coastline, Figures 6d and 6e), shows that most of the differences are due to the offshore assumptions. The moment rate per unit length below land, where GPS, tide, and leveling data exist, is relatively well constrained and is similar for both modeling assumptions (Figures 6c–6e). Modeled moment rates per unit length diverge north of 49°N, but the number of observations there is substantially reduced (Figures 4, 5, and 6e).

A broad transition zone in central Oregon is consistent with prior results presented in *McCaffrey et al*. [2007] and *McCaffrey et al*. [2013]. Using a Gamma-like model with gamma fixed so that a narrow locking transition zone is forced, *Burgette et al*. [2009] estimate that the bottom of the transition zone is shifted offshore in central Oregon. *McCaffrey et al*. [2013] note the discrepancy between modeled transition zones in central Oregon, and determined that allowing gamma to vary so that a wide transition zone is allowed fits the horizontal GPS data better. In either case (allowing a wide transition zone, or fixing it), information is garnered regarding the along-strike variation in locking—i.e., locking between 43°N and 46°N either has to have a wide transition zone or must be moved updip, away from the coastline in order to fit the observed reduced interseismic uplift rates. Locking between 40°N and 43°N has a narrow transition zone positioned further west than central Cascadia, except at 41°N in northern California where the locking pattern broadens (Figures 6a and 6b). Our Gaussian model with the revised plate geometry also shows a broad zone of locking at 41°N and between 43°N and 46°N (Figure S5).

Table 3. Model Fit Statistics

Model	Nd[a]	Np[a]	Reduced χ^2 (χ^2/(Nd-Np-1)	Reduced χ^2 + Penalties	Horizontal NRMS[a]	Vertical NRMS[a]
Gaussian Decade scale	1727	141	1.55	1.72	PA: 1.49 PB: 1.39	PA: 0.98 PB: 1.40 BU: 0.69
Gamma Decade scale	1727	141	1.61	1.74	PA: 1.50 PB: 1.48	PA: 1.33 PB: 1.33 BU: 0.67
SSE	239,715	756	1.31	1.88	PA: 1.07 PB: 1.29	PA: 1.10 PB: 1.06

[a]Number of data (Nd), number of adjustable parameters (Np), and Normalized Root-Mean-Square (NRMS). NRMS is estimated for PANGA (PA) and PBO (PB) data sets separately.

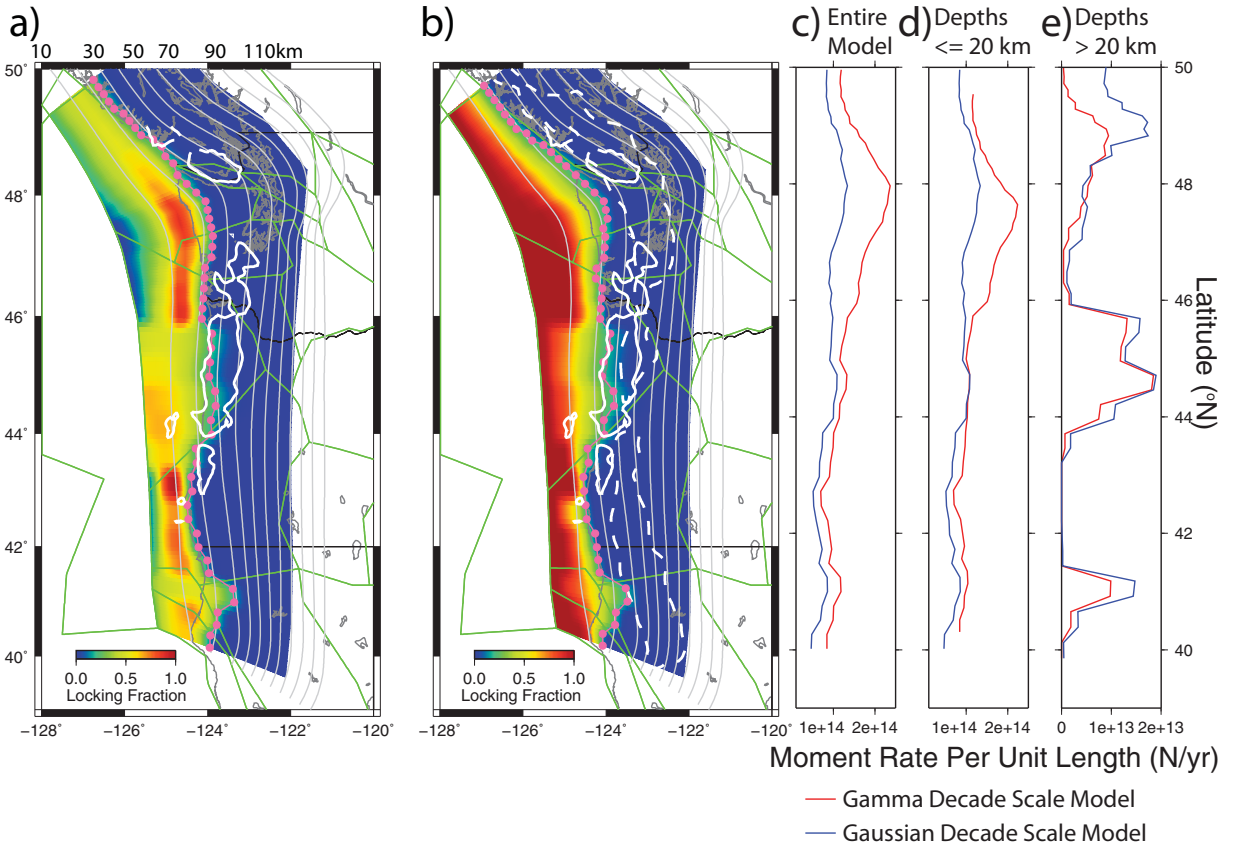

Figure 6. Maps of (a) Gaussian and (b) Gamma decade-scale model locking fraction with pink dotted line that marks the downdip 20% locked contour. Solid white lines mark the 10 mgal gravity anomaly contour of *Blakely et al.* [2005] (Figure 1b). Dashed white line (Figure 6b) indicates where 96% of tremors are located from the PNSN catalog between 2009 to 2012. Green lines mark modeled plate boundaries and thin gray lines are 10 km depth contours from *McCrory et al.* [2004] (labeled in Figure 6a). Moment rate per unit length for the Gamma (red line) and Gaussian (blue line) models (c) and for depths $<=$ 20 km (d) and $>$20 km (e) are shown.

To elucidate differences in models that use only horizontal or only vertical decade-scale velocities, we explore how our locking estimate would change if we give vertical GPS velocities higher weight. We multiply GPS vertical velocity uncertainties by 0.1 (increasing the weight by 100) and run the Gaussian decade-scale model with the adjusted weights (Figures S6–S8). Models that include higher weights for vertical GPS measurements have reduced vertical residuals in northern California (Figure S7) resulting in an increased locking fraction south of 41°N (Figure S8). Similar to the unmodified Gaussian decade-scale model, the plate interface offshore Oregon has a wider locking transition zone relative to the north and south. We prefer, however, our original decade-scale models with no vertical weighting adjustments since those models use more realistic data uncertainties.

4.2. SSE Model Results

The SSE model estimates inter-SSE locking, plate rotations, strain rates in the YFTB, ECCR, and WCCR blocks, 16 slow-slip events and one earthquake with a reduced χ^2 of 1.31 (Figures 7a–7c and S9, Tables 2 and 3, and supporting information tables). It matches well temporal and spatial variations in GPS time series, periods of elevated tremor (Figures 2, 3, S9, and S10), and displacements from the 2010 Eureka earthquake (Figure S11 and Tables 1 and 4). We estimate a similar earthquake moment magnitude (Mw 6.7), strike, and latitude to the Berkeley seismic solution (Figure S11 and Table 4). Differences between inter-SSE and decade-scale GPS velocities are shown in Figures S12a–S12c. Larger eastward inter-SSE velocities imply more inter-SSE locking (Figures S13a–S13c). Inter-SSE locking is shifted eastward compared to decade-scale locking and is weaker between 43°N and 46°N. The starting locking parameters assume the peak of Gaussian locking is at 30 km depth, which is then adjusted in the model inversion. We test this result by running a model with an initial inter-SSE peak Gaussian locking depth of 10 km. The new model produces shallow

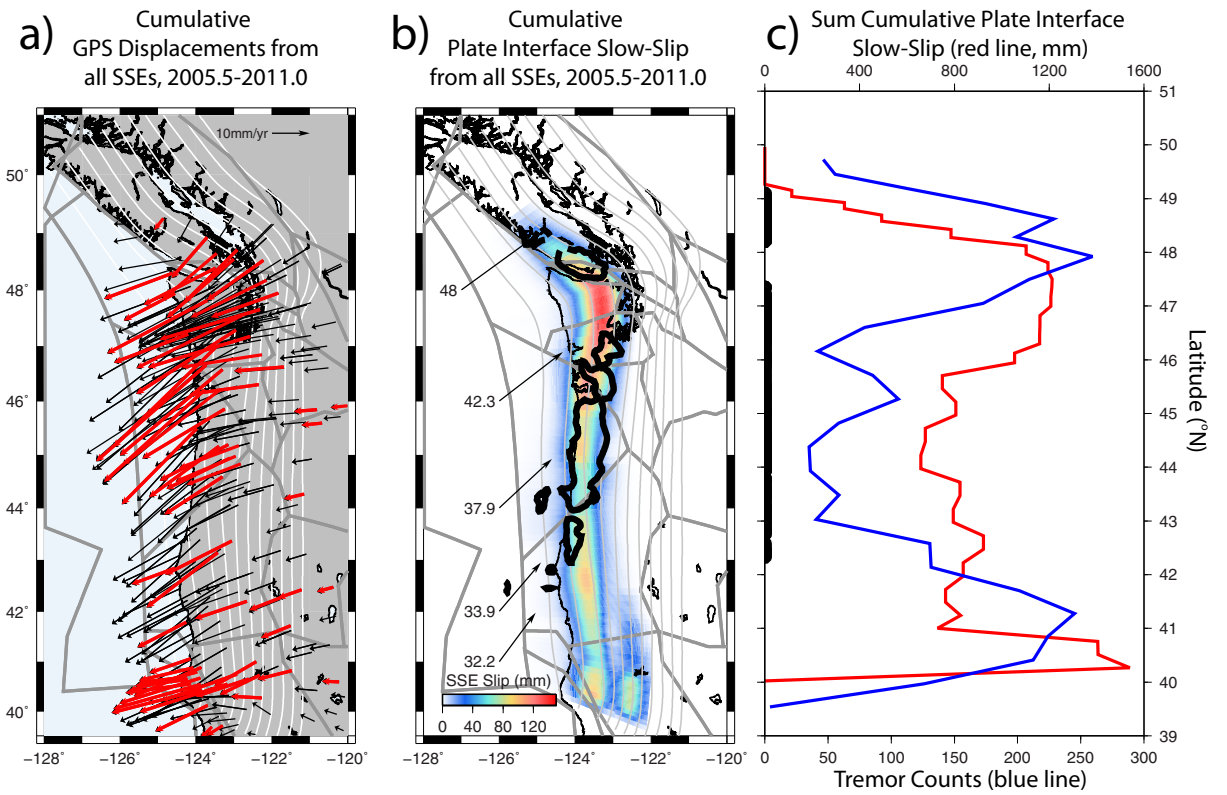

Figure 7. (a) Distribution of cumulative slow-slip displacements detected by continuous GPS from 2005.5 to 2011.0 (black vectors). Red vectors mark sites that were operating for 90% or more of the study time period. Near-vertical light gray lines are 10 km depth contours from *McCrory et al*. [2004] and dark gray lines are modeled blocks. (b) Summed plate interface slow-slip from 2005.5 to 2011. Black vectors are North America relative convergence rates and directions. Thick, solid black lines mark the 10 mgal gravity anomaly contour of *Blakely et al*. [2005]. (c) Cumulative node depth profile interface slow-slip from 2005.5 to 2011 (red line) and 50 km binned cumulative tremor counts from 2009.8 to 2013.0 acquired from the PNSN tremor catalog (blue line). Thick black line represents latitudes with high gravity anomalies.

locking with a reduced χ^2 of 1.38, compared to a reduced χ^2 of 1.31 obtained by the deeper inter-SSE locking model given the same number of data and free parameters.

Our geodetic moments of SSEs are systematically higher than those estimated by *Schmidt and Gao* [2010] (Table 2; using the same rigidity of 40 GPa). One reason *Schmidt and Gao* [2010] may estimate smaller moments is because their model accounts for only dip-slip motion whereas we include strike-slip. Their assumption is likely valid north of Portland where the plate convergence vector is parallel to the fault dip. Further south, however, plate convergence is oblique and SSEs include some oblique slip. *Schmidt and Gao* [2010] limit their analysis to north of 45.5°N in Oregon and south of 49.5°N on Vancouver Island. Our model is not so limited and picks up slip over a larger region, increasing the possible slip area and therefore the moment (Figure S10). We allow a wide Gaussian slip distribution, which may also contribute to larger geodetic moments. Another reason our moments are larger is because our model may not discriminate between events that are close in space and time. Since we are interested in the total slip for the margin as a function of latitude, it is not important to discriminate between events closely spaced in time, rather it is more important the inter-SSE velocity be correctly approximated so that the total slow-slip displacement for that time period can be estimated.

Table 4. Geodetic and Berkeley (BRK) Seismic Solution Parameters for the 9 January 2010 Earthquake

Parameter	Geodetic	BRK
Mo[a] (Nm)	1.41×10^{19}	7.1×10^{18}
Mw[a]	6.7	6.5
Slip Amplitude (mm)	550.9	N/A
Strike (°CW from N)	222.5	230.0
Latitude (°N)	40.63	40.65

[a]Moment (Mo) and Moment Magnitude (Mw).

The SSE model predicts slow-slip well inland in southern Cascadia, south of 41°N, coincident with a broader zone of locking (Figures 6, 7, and S10). Tectonic tremor is also located farther east in this section of the subduction zone (Figure 6b). In this region, new estimates of the plate interface reveal a shallow dipping geometry that extends inland under northern California

[*McCrory et al*., 2012], indicating the plate interface depth at which ETS is observed extends further east in this region.

Cumulative slow-slip from all major SSE events from 1 July 2005 to 1 January 2011 show the largest observed cumulative SSE GPS displacements and plate interface slow-slip occur below Washington, peaking at about 48°N, and in northern California, south of 41°N (Figures 7a–7c, see Figure S10 for individual slow-slip events). Cumulative slow-slip south of 43°N does not substantially increase until south of ~41°N (Figure 7b), although a small increase in slow-slip is observed between 42°N and 43°N (Figure 7b). PNSN tectonic tremor counts from 1 August 2009 to 30 July 2013 show a similar pattern as slow-slip (Figure 7c), but with elevated tremor from 40°N to 43°N and 46°N to 49°N, and less tremor between 43°N and 46°N. Differences in patterns of slow-slip and tectonic tremor may be due to differences in observed time periods (1 July 2005 to 1 January 2011 for cumulative slow-slip and 1 August 2009 to 30 July 2013 for cumulative tremor). The dearth of slow-slip relative to the large amount of tremor from 41°N to 43°N seems to be real since the model fit to the time series indicates that we did not miss a large event (Figures 3a, 3b, and 7a–7c).

4.3. Distribution of Terranes

The Metchosin, Crescent, and Siletz terranes are composed of thick accumulations of ~52–50 Ma (Eocene age) oceanic basalt found in southern Vancouver Island, western Washington, and western Oregon, respectively. We refer to all three terranes collectively as the "Siletzia." We use the Bouguer (onshore) and free-air (offshore) gravity anomalies presented in *Blakely et al*. [2005] to map thick accumulations of the dense Siletzia terrane (Figure 1b). Gravity anomalies and seismic profiles suggest that the Siletzia is present in the Coast Ranges north of 43°N [*Trehu et al*., 1994; *Blakely et al*., 2005; *Parsons et al*., 2005]. *Trehu et al*. [1994] use a north-south seismic profile to infer that the Siletzia terrane is ~27 km thick in central western Oregon, thins to ~20 km in northern Oregon, ~10 km in northern Washington and ~6 km offshore Vancouver Island. Their east-west seismic profile north of Corvallis, OR at about 45°N shows that the Siletzia terrane extends to ~35 km offshore where it is truncated by a fault (see their Figure 4). Their estimated maximum thickness of Siletzia terrane abuts the subducting plate near the coast [*Trehu et al*., 1994]. In map view, the Siletzia terrane extends offshore between ~43°N and 46°N and at latitudes >48°N [*Snavely*, 1987]. *Parsons et al*. [2005] seismically image the Siletzia terrane offshore near 46°N, but then image it east of the Olympics near Puget Sound at about 48°N. Siletzia terrane is seismically imaged east of the Cascades [*Schmandt and Humphreys*, 2011], but we focus on the thick accumulations above the plate interface, since these are more likely to influence current subduction zone processes. Contours of the gravity anomalies (10 mgal, Figure 1b) show that the Siletzia terrane may be broken into distinct blocks [*Blakely et al*., 2005]. The largest range from 44°N to 46°N and smaller fragments are observed north and south of it. The large gravity anomaly is notably absent over the Olympics, where the Siletzia has been pushed eastward toward the Puget Sound region (Figure 1b).

A significant decrease in seismicity occurs south of 47°N, in the transition from the Olympic accretionary complex (Figure 1c) to the Siletzia terrane [*McCrory et al*., 2004]. High seismic wave speeds and earthquakes that follow the edges of the Siletzia terrane indicate that it is relatively rigid compared to its surroundings [*Parsons et al*., 2005]. Because of its oceanic affinity, the Siletzia terrane may have reduced crustal porosity and permeability [*Calkins et al*., 2011]; however, it may be highly fractured at depth, which could increase its permeability. To our knowledge, no study has directly measured the porosity and permeability of the Siletzia terrane in comparison to the adjacent Olympic accretionary wedge or Klamath Mountains.

Under the Olympic Mountains in northwest Washington, the subduction plate interface changes from east plunging south of 47°N to northeast plunging north of the Puget Sound [*Crosson and Owens*, 1987; *McCrory et al*., 2004; *Audet et al*., 2010]. This bend in the subduction zone has been attributed to the extension in the Basin and Range province 16–18 million years ago that forced a clockwise, northward rotation of the Coast Ranges and the subduction zone, causing the exhumation of the Olympic Mountains accretionary complex since ~14 Ma [*Brandon et al*., 1998; *Wells et al*., 1998]. The Olympic accretionary complex is characterized by low seismic wave speeds indicating that the sediments are less consolidated (i.e., increased porosity) relative to Siletzia terrane and/or that the crust is fluid rich [*Parsons et al*., 2005; *Calkins et al*., 2011; *Calvert et al*., 2011]. The accretionary complex is composed of nonmagnetic material compared to its surroundings, and is well imaged using a magnetic potential field (Figure 1c) [*Blakely et al*., 2005]. The pre-Tertiary Klamath mountains are composed of multiple accretionary episodes [*Irwin*, 2003]. Gravity data that cover northern

California and southern Oregon between 39°N and 43°N [e.g., *Riddihough et al*., 1986] do not reveal a large anomaly near the Klamath Mountains, indicating that the accreted terrane is either less dense, less thick or has a deep root. Hence, the Klamath Mountains, in contrast to the denser and stronger Siletzia terrane, are interpreted to be lighter and weaker [*Brudzinski and Allen*, 2007].

The similarity in moment rates per unit length between the Gaussian and Gamma decade-scale models at depths >20 km (Figure 6e) suggests that our present day geodetic observations contain information regarding along-strike variations in locking. Although the models are not unique, the concurrence of a wide locking transition zone with the Siletzia terrane may imply that the upper plate composition contributes to the frictional interplate locking [*Burgette et al*., 2009] (Figures 6a, 6b, and S6). *Brudzinski and Allen* [2007] note that regions with more frequent ETS occur where the Siletzia terrane is thinned or absent. Likewise, our SSE model shows that cumulative GPS slow-slip displacements, plate interface slow-slip, and tectonic tremor distributions anticorrelate with the location of Siletzia terrane (Figures 7a–7c).

Paleoseismic estimates of coseismic subsidence from the the most recent major earthquake on the Cascadia subduction zone (A.D. 1700) [e.g., *Atwater et al*., 2005] have been used to estimate the distribution of coseismic slip on the fault [*Leonard et al*., 2004, 2010; *Wang et al*., 2013]. Recent improvements in subsidence estimates of the 1700 earthquake from detailed tidal microfossil studies allow *Wang et al*. [2013] to infer a heterogeneous displacement pattern along the margin of the subduction zone. In general, however, subsidence is smaller between 43.5°N and 46°N, in the same region as the large gravity anomalies (Figure 5b). *Wang et al*. [2013] have no observations between 47°N and 49°N, nor from 41°N to 42.5°N, but estimates near 43°N and 47°N suggest that subsidence was greater ($\sim\geq$1 m, Figure 5b) in these regions.

Leonard et al. [2010] compile a 6500 year coseismic subsidence record that shows less subsidence for multiple events between 44°N and 46°N. Specifically, their events T1, T3, T4, T5, T6, T7, and T9 (corresponding to events at approximately 300, 850, 1250, 1650, 2550, 3150, and 4150 years before 2000 A.D.) indicate less subsidence between 44°N and 46°N. These results suggest that coseismic subsidence in central Oregon at about 44°N–46°N (in the region of the thickest accumulations of Siletzia terrane) is consistently lower in subduction earthquakes.

5. Discussion

We present two schematic profiles across the margin to summarize the observations of this paper. The Olympic profile runs through the Olympic Mountains and Puget Sound following the direction of relative plate convergence (Figure 8a), and is roughly based on the geologic profile presented in *Stanley et al*. [1999]. The Oregon profile passes through central Oregon and the Willamette Valley (Figure 8b) and is based on the profile presented in *Blakely et al*. [2005]. The Olympic profile (Figure 8a) is characterized with strong locking offshore and a relatively narrow transition zone (Figures 6a and 6b), elevated tectonic tremor and slow-slip (Figures 7b and 7c), and possible large subsidence during earthquakes (Figure 5b). The profile goes through the Olympic accretionary wedge (Figure 1c), which is inferred to be fluid rich from seismic studies [*Calkins et al*., 2011]. Gravity anomalies are low in this area, suggesting that the dense Siletzia terrane is thin or absent near the coast (Figure 1b). Using seismic data, *Parsons et al*. [2005] show that the Siletzia terrane is present further east in this profile, under the Puget Sound.

The Oregon profile (Figure 8b) is characterized by a wide transition zone (Figures 6a and 6b), reduced amounts of cumulative slow-slip, tectonic tremor (Figures 7b and 7c), and coseismic subsidence (Figure 5b). Strong gravity anomalies (Figure 1b) suggest the thickest accumulations of the dense Siletzia terrane are here. The Oregon profile has a strong magnetic anomaly [*Blakely et al*., 2005] while magnetic anomalies across the Olympic profile are weak or absent (Figure 1c).

The coast at about 41°N has substantial vertical interseismic uplift (Figures 5h and S3) and a wide transition zone (Figures 6a, 6b, and S5). In this region, the fault interface is shallow and dips gently under northern California (Figure S5). We suggest that the broad zone of locking in this region is related to the low dip angle of the plate interface.

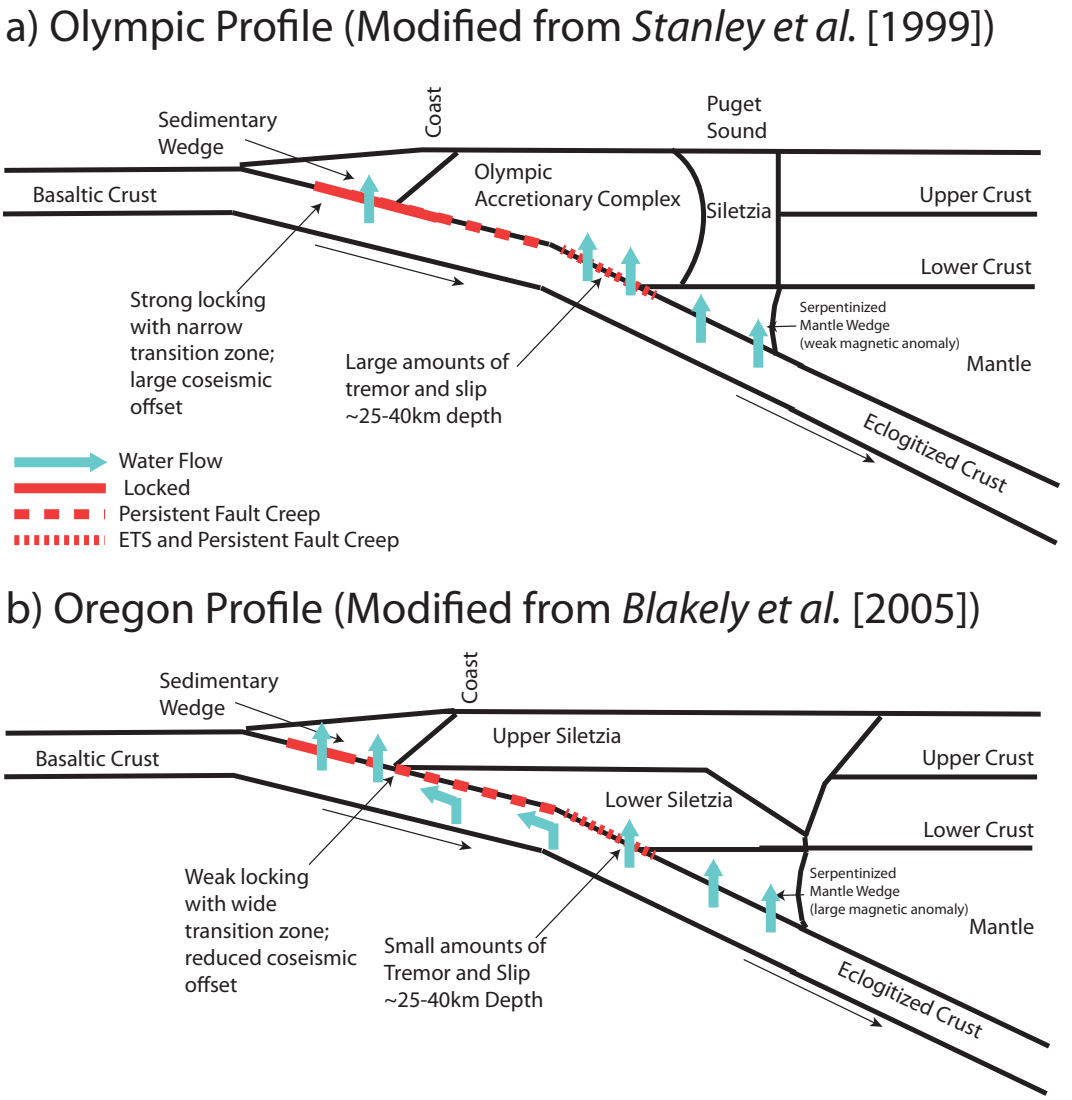

Figure 8. Schematic illustrating observations. (a) In the Olympic profile generalized from *Stanely et al.* [1999], a strong locking fraction and a thinner locking transition zone are estimated updip of elevated cumulative slow-slip and tectonic tremor. Although there are few observations, existing coseismic subsidence records are large (~1–2 m). Gravity anomalies are low, suggesting decreased amounts of Siletzia terrane. (b) In the Oregon profile modified from *Blakely et al.* [2005], the locking fraction is weaker and characterized with a wide locking transition zone. Tectonic tremor and cumulative slow-slip are depressed. Large gravity anomalies suggest the presence of the dense Siletzia terrane.

The section of the subduction zone between 43°N and 46°N has reduced interseismic uplift, coseismic subsidence, and an estimated broad locking transition zone (Figures 5, 6a, 6b, S3, and S5). Unlike northern California this region does not have a shallow dipping fault interface. Using body wave tomography, *Schmandt and Humphreys* [2010] observed that the high-velocity slab becomes weak to nonexistent beneath northern Oregon at depths greater than ~160 km. In contrast, slab depths continue to ~350 km to the north and south. Variations in slab pull could provide a mechanism for the observed locking pattern, however, *Scholz and Campos* [1995], suggest that reduced slab pull should *increase* coupling, which is opposite of what is observed in central Cascadia.

Alternatively, reduced interseismic uplift and coseismic subsidence may suggest that prolonged partial fault creep prevents accumulation of large interseismic stress, thereby reducing coseismic offsets (Figures 9a and 9b). *Meade and Loveless* [2009] suggest that geodetically constrained estimates of apparent partial locking on subduction zone interfaces worldwide may be due to ongoing Mw $\geq$ 8 silent earthquakes with durations of decades to centuries. If the predicted slip velocity of great SSEs is temporally steady and slower than the

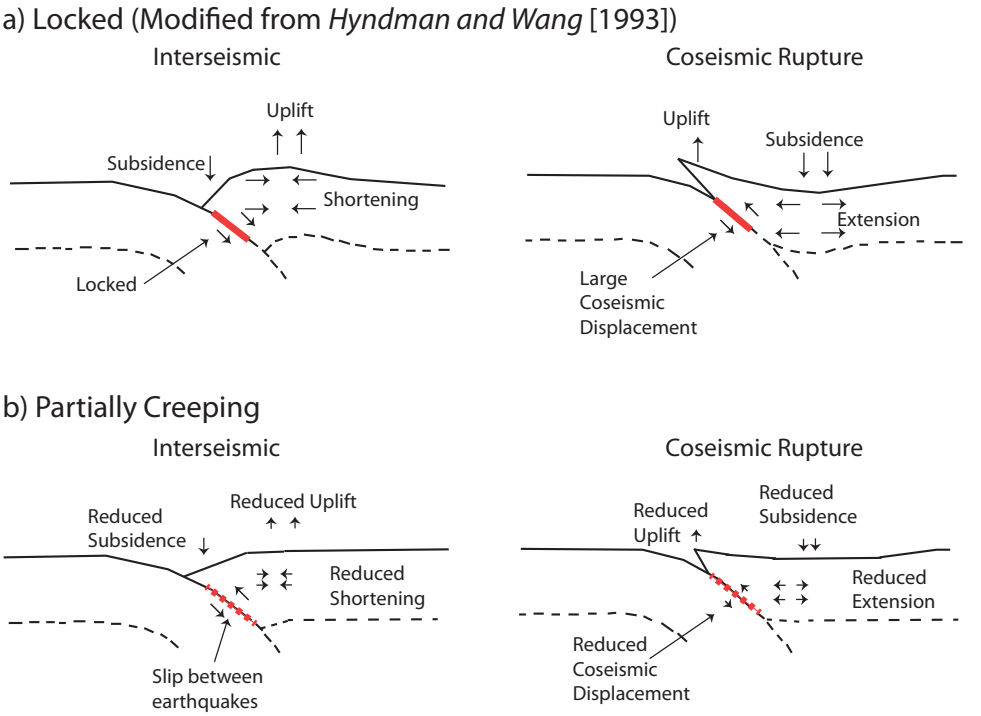

Figure 9. Schematic diagrams based on *Hyndman and Wang* [1993] showing crustal deformation in between major earthquakes (left) and during rupture (right) for a fully locked fault (a) and a partially creeping fault (b). Interseismic uplift and coseismic subsidence are reduced in regions with partial persistent fault creep.

plate convergence rate (<50 mm/yr in Cascadia) and durations are longer than the observation period (>10 years) then these events will not be observable in geodetic time series. Such great SSEs may simply reduce the accumulating strain rate, creating the appearance of a partially coupled (or creeping) subduction zone, similar to what is observed in central Oregon (Figure 6). However, observed SSEs that last months to years generally show complexity in their slip evolution (changing slip rates and migration) and we expect a M $\geq$8 SSE would have similar properties, which would be observable. Cascadia SSEs are all short in duration and there is no evidence for longer-period slip variations. Hence, it is possible but untestable and unlikely that this region is undergoing a great SSE.

Coastal coseismic displacements measured from paleoelevation studies reveal that the greatest coastal subsidence (up to ~2 m) during the 1700 earthquake, as well as during previous subduction earthquakes within a 6500 year history, occurred north of 46°N and south of 44°N [*Leonard et al*., 2004, 2010; *Wang et al*., 2013]. The least subsidence for multiple events occurred in central to northern Oregon (<1m) [*Leonard et al*., 2010], in the region where we and *McCaffrey et al*. [2013] estimate a wide locking transition zone (Figures 6a and 6b). Consistent with the paleoseismic observations, a morphometric analysis of submarine landslides on the continental slope of Oregon indicates a lack of disintegrative landslides in northern Oregon where sedimentation rates are high due to the influx of the Columbia River system, suggesting that shaking from great earthquakes is limited in this region [*McAdoo and Watts*, 2004]. Tsunami deposits in the southern Cascadia margin, however, may have been generated from earthquakes or submarine landslides, or a combination of both [*McAdoo and Watts*, 2004]. Because paleoseismic evidence reveals persistent reduced subsidence for multiple earthquakes within a 6500 year history between 44°N and 46°N, we suggest that central Cascadia between 44°N and 46°N is prone to continuous partial fault creep.

We note that the region of continuous fault creep coincides with the thickest accumulations of the Siletzia terrane and suggest the permeability of the terrane provides a mechanism for persistent fault creep. *Reyners and Eberhardt-Phillips* [2009] suggest a conceptual locking model for the Hikurangi Subduction Zone (HSZ) below North Island, New Zealand that involves fluids derived from the basalt-eclogite transition moving

updip beneath the stronger, less permeable Rakaia terrane, increasing pore fluid pressures on the plate interface and within the upper part of the subucting slab. The transported water is later released into the more permeable Pahau terrane further updip, ultimately effecting the locking beneath the Rakaia and updip. In Cascadia, the Siletzia terrane may also act as an impermeable cap, where some of the water moves updip since it cannot percolate into the overriding crust. In central Oregon, the Siletzia terrane extends to ~35 km offshore, possibly allowing fluid transport further updip into the locked region. Here we observe less interseismic uplift that may be due to weak locking (creep) accommodating interseismic stress, resulting in reduced coseismic offsets (Figures 8 and 9). Hence, high fluid pore pressures may promote creep beneath the Siletzia terrane since these conditions are thought to favor stable sliding [*Segall and Rice*, 1995; *Hillers and Miller*, 2006].

Similar to the results of *Brudzinski and Allen* [2007], we show reduced slow-slip for the time period of this study between ~41°N and 46°N and reduced tremor between ~43°N and 46°N, in the region where thick accumulations of the Siletzia terrane extend offshore (Figures 6b and 7a–7c). Tectonic tremor and slow-slip have also been explained by dewatering from the basalt-eclogite transition of the subducting crust at about 40 km depth [*Bostock et al*., 2002] where they are observed. *Audet et al*. [2010] suggest that fluids trapped beneath a seal at the plate boundary increase pore fluid pressures and lower the effective stress enough to trigger slip by small changes in dynamic stress. Propagating slip and hydrofracturing the seal allow fluid to flow into the overriding plate or along the interface, enhancing ETS propagation. Fluid pumping during slip episodes decreases pore fluid pressure and increases the effective stress, stopping the slow-slip and reinforcing the new seal. *Audet et al*. [2010] suggest that variations in rates of slab dehydration, permeability and rheology of the upper crust contribute to variations in ETS recurrence. Hence, if the Siletzia terrane is less permeable, it may offer a stronger seal than in adjacent regions to the north and south, implying less frequent ETS events, as observed. Assuming the same rate of dewatering along the plate margin, this would also imply larger pore pressures, which, as described above, would encourage prolonged partial creep.

SSEs accommodate much of the subduction slip in Washington, southern Oregon and northern California, but in central and northern Oregon that amount is greatly reduced and may instead be accommodated through persistent partial fault creep. If persistent partial fault creep occurred only updip of the ETS zone, then the load on the fault in the ETS zone would increase and foster more ETS events. We observe, however, that ETS in Cascadia reduces where partial fault creep is larger. Hence, we argue that persistent partial fault creep must extend through the ETS zone. ETS is also thought to be promoted by high fluid pore pressure. So, as fluid pressure increases due to a better seal, perhaps persistent partial fault creep becomes the dominant mode of slip, even in the ETS zone. *Peng and Gomberg* [2010] suggest that the mode of slip is determined by the inherent properties of the fault surface. If correct, the physical properties of the Siletzia and adjacent terranes may determine if the interface slips as ETS, persistent fault creep or as earthquakes.

6. Conclusions

Along-strike variations in Cascadia subduction locking using GPS decade-scale velocities (uncorrected for slow-slip) and tide gauge and leveling uplift rates suggest a broadly distributed zone of locking between 43°N and 46°N. Coseismic subsidence inferred from paleoelevation studies is reduced between 44°N and 46°N for earthquakes within a 6500 year history. Persistent partial fault creep explains these observations. Gravity anomalies inferred to reveal thick accretions of Siletzia terrane between 43°N and 46°N coincide with reduced interseismic uplift and coseismic subsidence. If the Siletzia terrane is impermeable, then high pore fluid pressures near the fault interface may encourage persistent fault creep. Cumulative slow-slip from 2005.5 to 2011 derived from three-component GPS position time series and tectonic tremor counts are also lowest between ~43°N and 46°N. Terrane properties may influence the mode of slip, where slow-slip and tremor are encouraged with permeable terranes, and persistent fault creep with impermeable terranes. Reduced interseismic uplift and paleoseismic coseismic subsidence between 43°N and 46°N suggest that central Cascadia will slip less than regions to the north and south during future great earthquakes, therefore impacting seismic hazard along the margin.

Acknowledgments

This work was funded by the National Science Foundation (NSF) Postdoctoral Fellowship Program, award 0847985 (Schmalzle), NSF award EAR-1062251 (McCaffrey), and USGS National Earthquake Hazards Reduction Program, Award G12AP20033 (Schmalzle and Creager). Many thanks to Reed Burgette and an anonymous reviewer for their thoughtful comments and suggestions that greatly improved this paper. Thanks to Mike Brudzinski and Aaron Wech for providing their tremor catalogs. Thanks to Rick Blakeley for providing aeromagnetic and gravity data. Craig H. Faunce provided assistance with R programing. Bruce Nelson, Steve Malone, Justin Sweet, David Schmidt, Aaron Wech, Tom Pratt, Brian Atwater, Sarah Minson, Lorraine Wolf, and Aimee Schmalzle provided useful comments and insight. Thanks to PBO and PANGA for providing access to GPS data products. All figures were made with GMT, R, and Adobe Illustrator.

References

Anderson, G., K. Hodgkinson, T. A. Herring, and D. C. Agnew (2006), *Plate Boundary Observatory Data Management System Critical Design Review*, Version 1.2.

Atwater, B. F., M.-R. Satoko, S. Kenji, T. Yoshinobu, U. Kazue, and D. K. Yamaguchi (2005), *The Orphan Tsunami of 1700: Japanese Clues to a Parent Earthquake in North America*, edited by U.S. Geological Survey, U.S. Geol. Surv. and Univ. of Wash. Press.

Atwater, T. (1970), Implications of plate tectonics for the Cenozoic tectonic evolution of western North America, *Geol. Soc. Am. Bull.*, *81*(12), 3513–3535.

Audet, P., M. Bostock, D. C. Boyarko, M. R. Brudzinski, and R. M. Allen (2010), Slab morphology in the Cascadia fore arc and its relation to episodic tremor and slip, *J. Geophys. Res.*, *115*, B00A16, doi:10.1029/2008JB006053.

Blakely, R. J., T. M. Brocher, and R. E. Wells (2005), Subduction-zone magnetic anomalies and implications for hydrated forearc mantle, *Geology*, *33*(6), 445–448, doi:10.1130/G21447.1.

Bostock, M. G., R. D. Hyndman, S. Rondenay, and S. M. Peacock (2002), An inverted continental Moho and serpentinization of the forearc mantle, *Nature*, *417*, 536–538.

Boyarko, D. C., and M. R. Brudzinski (2010), Spatial and temporal patterns of nonvolcanic tremor along the southern Cascadia subduction zone, *J. Geophys. Res.*, *115*, B00A22, doi:10.1029/2008JB006064.

Brandon, M. T., M. K. Roden-Tice, and J. I. Garver (1998), Late Cenozoic exhumation of the Cascadia accretionary wedge in the Olympic Mountains, northwest Washington State, *Geol. Soc. Am. Bull.*, *110*(8), 985–1009.

Brudzinski, M. R., and R. M. Allen (2007), Segmentation in episodic tremor and slip all along Cascadia, *Geology*, *35*(10), 907–910.

Burgette, R. J., R. Weldon, and D. A. Schmidt (2009), Interseismic uplift rates for western Oregon and along strike variation in locking on the Cascadia subduction zone, *J. Geophys. Res.*, *114*, B01408, doi:10.1029/2008JB005679.

Burgmann, R., M. G. Kogan, V. E. Levin, C. H. Scholtz, R. W. King, and G. M. Steblov (2001), Rapid aseismic moment release following the 5 December 1997 Kronotsky Kamchatka earthquake, *Geophys. Res. Lett.*, *28*, 1331–1334.

Calkins, J. A., G. A. Abers, G. Ekstrom, K. C. Creager, and S. Rondenay (2011), Shallow structure of the Cascadia subduction zone beneath western Washington from spectral ambient noise correlation, *J. Geophys. Res.*, *116*, B07302, doi:10.1029/2010JB007657.

Calvert, A., L. A. Preston, and A. M. Farahbod (2011), Sedimentary underplating at the Cascadia mantle-wedge corner revealed by seismic imaging, *Nat. Geosci.*, *4*, 545–548, doi:10.1038/ngeo1195.

Crosson, R. S., and T. J. Owens (1987), Slab geometry of the Cascadia subduction zone beneath Washington from earthquake hypocenters and teleseismic converted waves, *Geophys. Res. Lett.*, *14*, 824–827, doi:10.1029/GL014i008p00824.

DeMets, C., and T. Dixon (1999), New kinematic models for Pacific-North America motion from 3 Ma to present. I: Evidence for steady motion and biases in the NUVEL-1A model, *Geophys. Res. Lett.*, *26*, 1921–1924.

Douglas, A., J. Beavan, L. Wallace, and J. Townend (2005), Slow slip on the northern Hikurangi subduction interface, New Zealand, *Geophys. Res. Lett.*, *32*, L16305, doi:10.1029/2005GL023607.

Dragert, H., K. Wang, and T. S. James (2001), A silent slip event on the deeper Cascadia subduction interface, *Science*, *292*(5521), 1525–1528.

Flück, P., R. D. Hyndman, and K. Wang (1997), Three-dimensional dislocation model for great earthquakes of the Cascadia subduction zone, *J. Geophys. Res.*, *102*, 20,539–20,550.

Freymueller, J. T., S. Hreinsdottir, C. Zweck, and P. J. Haeussler (2002), The 1998–2002 deep megathrust slip event, Alaska, *Eos Trans. AGU*, *83*(47), Fall Meet. Suppl., Abstract G61A-0972.

Heki, K., S. Miyazaki, and H. Tsuji (1997), Silent fault slip following an interplate thrust earthquake at the Japan Trench, *Nature*, *386*, 595–598.

Hillers, G., and S. A. Miller (2006), Stability regimes of a dilatant, fluid infiltrated fault plane in a three-dimensional elastic solid, *J. Geophys. Res.*, *111*, B08304, doi:10.1029/2005JB003872.

Hirose, H., K. Hirahara, F. Kimata, N. Fujii, and S. Miyazaki (1999), A slow thrust slip event following the two 1996 Hyuganada earthquakes beneath the Bungo channel, southwest Japan, *Geophys. Res. Lett.*, *26*, 3237–3240.

Hyndman, R. D., and K. Wang (1993), Thermal constraints on the zone of major thrust earthquake failure: The Cascadia subduction zone, *J. Geophys. Res.*, *98*, 2039–2060.

Irwin, W. P. (2003), Correlation of the Klamath Mountains and Sierra Nevada, *Open File Rep. 02–490*.

Leonard, L., R. D. Hyndman, and S. Mazzotti (2004), Coseismic subsidence in the 1700 great Cascadia earthquake: Coastal estimates versus elastic dislocation models, *Geol. Soc. Am. Bull.*, *116*(5–6), 655–670, doi:10.1130/B25369.1.

Leonard, L. J., C. A. Currie, S. Mazzotti, and R. D. Hyndman (2010), Rupture area and displacement of past Cascadia great earthquakes from coastal coseismic subsidence, *Geol. Soc. Am. Bull.*, *122*(11–12), 2079–2096, doi:10.1130/B30108.1.

Lowry, A. R., K. M. Larson, V. Kostoglodov, and R. Bilham (2001), Transient fault slip in Guerrero, southern Mexico, *Geophys. Res. Lett.*, *28*, 3753–3756.

McAdoo, B. G., and P. Watts (2004), Tsunami hazard from submarine landslides on the Oregon continental slope, *Mar. Geol.*, *203*, 235–245.

McCaffrey, R. (2002), Block rotations and plate coupling, in *Plate Boundary Zones*, edited by S. Stein and J. T. Freymueller, 425 pp., AGU, Washington D. C.

McCaffrey, R. (2005), Block kinematics of the Pacific-North America plate boundary in the southwestern United States from inversion of GPS, seismological, and geologic data, *J. Geophys. Res.*, *110*, B07401, doi:10.1029/2004JB003307.

McCaffrey, R. (2009), Time-dependent inversion of three-component continuous GPS for steady and transient sources in northern California, *Geophys. Res. Lett.*, *36*, L07304, doi:10.1029/2008GL036784.

McCaffrey, R., M. Long, C. Goldfinger, P. C. Zwick, J. L. Nabelek, C. K. Johnson, and C. Smith (2000), Rotation and plate locking at the southern Cascadia subduction zone, *Geophys. Res. Lett.*, *27*, 2117–3120.

McCaffrey, R., A. Qamar, R. King, R. E. Wells, G. Khazaradze, C. A. Williams, C. W. Stevens, J. J. Vollick, and P. C. Zwick (2007), Fault locking, block rotation and crustal deformation in the Pacific Northwest, *Geophys. J. Int.*, *169*, 1315–1340.

McCaffrey, R., R. W. King, S. Payne, and M. Lancaster (2013), Active tectonics of northwestern US inferred from GPS-derived surface velocities, *J. Geophys. Res.*, *118*, 709–723, doi:10.1029/2012JB009473.

McCrory, P. A., L. Blair, D. H. Oppenheimer, and S. R. Walter (2004), *Depth to the Juan de Fuca Slab Beneath the Cascadia Subduction Margin—A 3-D Model for Sorting Earthquakes*, Vol. 91, 22 pp., U. S. Geol. Surv.

McCrory, P. A., J. L. Blair, F. Waldhauser, and D. H. Oppenheimer (2012), Juan de Fuca slab geometry and its relation to Wadati-Benioff zone seismicity, *J. Geophys. Res.*, *117*, B09306, doi:10.1029/2012JB009407.

Meade, B. J., and J. P. Loveless (2009), Predicting the geodetic signature of Mw ≥ 8 slow slip events, *Geophys. Res. Lett.*, *36*, L01306, doi: 10.1029/2008GL036364.
Miller, M., D. J. Johnson, C. M. Rubin, H. Dragert, K. Wang, A. Qamar, and C. Goldfinger (2001), GPS_determination of along-strike variation in Cascadia margin kinematics: Implications for relative plate motion, subduction zone coupling, and permanent deformation, *Tectonics*, *20*, 161–176, doi:10.1029/2000TC001224.
Mitchell, C. E., P. Vincent, R. Weldon, and M. A. Richards (1994), Present-day vertical deformation of the Cascadia margin, Pacific Northwest, *J. Geophys. Res.*, *99*, 12,257–12,277.
Okada, Y. (1985), Surface deformation due to shear and tensile faults in a half space, *Bull. Seismol. Soc. Am.*, *75*, 1135–1154.
Okada, Y. (1992), Internal deformation due to shear and tensile faults in a half-space, *Bull. Seismol. Soc. Am.*, *82*, 1018–1040.
Outerbridge, K. C., T. H. Dixon, S. Schwartz, J. I. Walter, M. Protti, V. Gonzalez, J. Biggs, M. Thorwart, and W. Rabbel (2010), A tremor and slip event on the Cocos-Caribbean subduction zone as measured by a GPS and seismic network on the Nicoya Peninsula, Costa Rica, *J. Geophys. Res.*, *115*, B10408, doi:10.1029/2009JB006845.
Ozawa, S., M. Murakami, and T. Tada (2001), Time-dependent inversion study of the slow thrust event in the Nankai Trough subduction zone, southwestern Japan, *J. Geophys. Res.*, *106*, 787–802.
Parsons, T., et al. (2005), Crustal structure of the Cascadia fore arc of Washington, in *Earthquake Hazards of the Pacific Northwest Costal and Marine Region*, vol. 40, U.S. Geol. Surv., Reston, Va.
Peng, Z., and J. Gomberg (2010), An integrated perspective of the continuum between earthquakes and slow-slip phenomena, *Nat. Geosci.*, *3*, 599–607.
Reyners, M., and D. Eberhart-Phillips (2009), Small earthquakes provide insight into plate coupling and fluid distribution in the Hikurangi subduction zone, New Zealand, *Earth Planet. Sci. Lett.*, *282*, 299–305.
Riddihough, R., C. Finn, and R. Couch (1986), Klamath-Blue Mountain lineament, Oregon, *Geology*, *14*, 528–531.
Rogers, G., and H. Dragert (2003), Episodic tremor and slip on the Cascadia subduction zone: The chatter of silent slip, *Science*, *300*, 1942–1943.
Romano, F., A. Piatanesi, S. Lorito, N. D'Agostino, K. Hirata, S. Atzori, Y. Yamazaki, and M. Cocco (2012), Clues from joint inversion of tsunami and geodetic data of the 2011 Tohoku-oki earthquake, *Sci. Rep.*, *2*, 385, doi:10.1038/srep00385.
Savage, J. C., W. J. Gan, and J. L. Svarc (2001), Strain accumulation and motion in the Eastern California Shear Zone, *J. Geophys. Res.*, *106*, 21,995–22,007.
Schmandt, B., and E. D. Humphreys (2010), Complex subduction and small-scale convection revealed by body-wave tomography of the western United States upper mantle, *Earth Planet. Sci. Lett.*, *297*, 435–445, doi:10.1016/j.epsl.2010.06.047.
Schmandt, B., and E. D. Humphreys (2011), Seismically imaged relict slab from the 55 Ma Siletzia accretion to the northwest United States, *Geology*, *39*, 175–178.
Schmidt, D. A., and H. Gao (2010), Source parameters and time-dependent slip distributions of slow slip events on the Cascadia subduction zone from 1998 to 2008, *J. Geophys. Res.*, *115*, B00A18, doi:10.1029/2008JB006045.
Scholz, C. H., and J. Campos (1995), On the mechanism of seismic decoupling and back arc spreading at subduction zones, *J. Geophys. Res.*, *100*, 22,103-22,115.
Schwartz, S., and J. M. Rokosky (2006), Slow slip events and seismic tremor at circum-Pacific subduction zones, *Rev. Geophys.*, *45*, RG3004, doi:10.1029/2006RG000208.
Segall, P., and J. R. Rice (1995), Dilatancy, compaction, and slip instability of a fluid-infiltrated fault, *J. Geophys. Res.*, *100*, 22,155–22,157.
SNARF Working Group (2004), *Stable North America Reference Frame*, Earthscope, Natl. Sci. Found. http://www.unavco.org/community_science/workinggroups_projects/snarf/SNARF1.0/SNARF1.0.html
Snavely, P. D. (1987), Tertiary geologic framework, neotectonics, and petroleum potential of the Oregon-Washington Continental Margin, in *Geology and Resource Potential of the Continental Margin of Western North America and Adjacent Ocean Basins—Beaufort Sea to Baja California*, edited by D. W. Scholl, A. Grantz, and J. G. Vedder, Springer, New York.
Stanley, D., A. Villasenor, and H. Benz (1999), Subduction zone and crustal dynamics of western Washington: A tectonic model for earthquake hazards evaluation, *Open File Rep. 99-0311, U.S. Geol. Surv.*, Denver, Colo.
Szeliga, W., T. Melbourne, M. Santillan, and M. Miller (2008), GPS constraints on 34 slow slip events within the Cascadia subduction zone, 1997–2005, *J. Geophys. Res.*, *113*, B04404, doi:10.1029/2007JB004948.
Trehu, A. M., I. Asudeh, T. M. Brocher, J. H. Luetgert, W. D. Mooney, J. L. Nabelek, and Y. Nakamura (1994), Crustal architecture of the Cascadia forearc, *Science*, *266*, 237–243.
Wang, K., S. Mazzotti, R. D. Hyndman, and T. Sagiya (2003), A revised dislocation model of interseismic deformation of the Cascadia subduction zone, *J. Geophys. Res.*, *108*(B1), 2026, doi:10.1029/2001JB001227.
Wang, P.-L., S. E. Engelhart, K. Wang, A. D. Hawkes, B. P. Horton, A. R. Nelson, and R. C. Witter (2013), Heterogeneous rupture in the great Cascadia earthquake of 1700 inferred from coastal subsidence estimates, *J. Geophys. Res.*, *118*, 2460–2473, doi:10.1002/jgrb.50101.
Wech, A. G. (2010), Interactive tremor monitoring, *Seismol. Res. Lett.*, *81*(4), 664–669.
Wech, A. G., and K. C. Creager (2008), Automated detection and location of Cascadia tremor, *Geophys. Res. Lett.*, *35*, L20302, doi:10.1029/2008GL035458.
Wech, A. G., and K. C. Creager (2011), A continuum of stress, strength and slip in the Cascadia subduction zone, *Nat. Geosci.*, *4*, 624–628, doi:10.1038/ngeo1215.
Wells, R. E., C. S. Weaver, and R. J. Blakely (1998), Fore-arc migration in Cascadia and its neotectonic significance, *Geology*, *26*(8), 759–762.
Wilson, D. S. (1993), Confidence intervals for motion and deformation of the Juan de Fuca plate, *J. Geophys. Res.*, *98*, 16,053–16,071.